PHYSICAL REVIEW B **86**, 144302 (2012)

Forced chemical mixing of immiscible Ag-Cu heterointerfaces using high-pressure torsion

M. Pouryazdan,[1,2] D. Schwen,[3] D. Wang,[1] T. Scherer,[1] H. Hahn,[1,2] R. S. Averback,[3] and P. Bellon[3]
[1]*Institute of Nanotechnology, Karlsruhe Institute of Technology (KIT), 76021 Karlsruhe, Germany*
[2]*Joint Research Laboratory Nanomaterials (KIT and TUD) at Technische Universität Darmstadt (TUD), Petersenstrasse 32, 64287 Darmstadt, Germany*
[3]*Department of Materials Science and Engineering, University of Illinois at Urbana-Champaign, 1304 W. Green Str., Urbana, Illinois 61801, USA*

(Received 20 June 2011; revised manuscript received 10 September 2012; published 1 October 2012)

Forced chemical mixing in nanostructured $Ag_{60}Cu_{40}$ eutectic alloys during severe plastic deformation by high-pressure torsion (HPT) was quantitatively studied using x-ray diffraction, differential scanning calorimetry, and transmission electron microscopy. Nearly complete chemical homogenization of the original lamellar structure with a wavelength of ≈ 165 nm was achieved after a shear strain of ≈ 350. The chemical mixing is accompanied by extensive grain refinement leading to nanocrystalline grains with average sizes of ≈ 42 nm. A Monte Carlo computer simulation model, which attributes mixing to dislocation glide, shows reasonable agreement with the experimental results. The model also shows that the characteristic strain for chemical homogenization scales linearly with the length scale of the system L, and not with the square of the length scale L^2, as would be expected for Fickian diffusion.

DOI: 10.1103/PhysRevB.86.144302 PACS number(s): 68.35.Fx, 07.35.+k, 81.40.−z, 05.10.Ln

I. INTRODUCTION

Mechanical alloying by severe plastic deformation (SPD), such as ball milling[1] or accumulative roll bonding (ARB),[2] has gained wide acceptance as a versatile means for processing nonequilibrium materials, for example alloys with extended solid solutions, amorphous alloys, and nanocomposites.[1] While these processing methods are quite straightforward to implement, the detailed process of how atoms intermix during SPD remains poorly understood.[3] In addition to its importance for processing of alloys, forced chemical mixing by SPD is also relevant more broadly in science and engineering: the homogenization of tribolayers in frictional wear,[4,5] the joining of metals by friction stir welding on the millimeter scale,[6] and even the reorganization of matter in the Earth's mantle on geological length scales.[7] The key unanswered question in all of these processes is how shear causes the redistribution of mass. In the present work we focus on forced chemical mixing at the atomic length scale by studying immiscible alloys. These alloys, as we will show, provide a convenient means for testing theoretical models of forced mixing. It is well recognized that SPD of many alloys that are immiscible in equilibrium can lead to complete solid solutions (e.g., Cu-Co,[8] Ag-Cu[9]), while in others, even cryomilling can extend solubilities by only small amounts (e.g., Ag-Ni,[10] Cu-Mo[11]). A number of different mechanisms have been suggested to explain these observations,[12–14] but these ideas have been largely qualitative in nature, with limited quantitative predictive capabilities.

Past studies have shown that during SPD of heterogeneous structures, such as the two-phase alloys noted above, the length scales of the inhomogeneities are greatly diminished by uniform deformation of the structure. For example, during ARB, stacks of different layers are made thinner in plane strain, before significant atomic mixing takes place at the interfaces.[15] A similar behavior occurs during wire drawing,[16] and high-pressure torsion,[17] while for ball milling the micron-sized powder particles are continuously flattened, fractured, and rebonded,[18] again reducing the length scale of the microstructure. During the early stages of these deformation processes, that is, strains less than ≈ 5, the interfaces remain relatively sharp, and the morphology distinctly two phase. With increasing strain, however, forced chemical mixing across interface boundaries becomes significant. At first the interfaces become diffuse, but eventually the entire alloy will homogenize. The current investigation considers the kinetics of this later homogenization process.

Part of the difficulty in advancing the understanding of forced chemical mixing processes derives simply from the lack of quantitative measurements on the dependence of intermixing on strain. Ball milling experiments, for example, are notably poor in this regard, and even crude estimates of the instantaneous strain rate, total strain, and local temperature of the powder during milling are generally not available.[18–20] ARB is far more controlled, but the total strain in this process is relatively small, less than ≈ 10. The processing variables during HPT are also well controlled, but in contrast to ARB, strains of over 1000 are readily possible, owing to large deformation of the sample with only minor changes in shape.[21] HPT, moreover, generates bulk, dense samples of macroscopic dimensions that are convenient for measurements of various properties. Recently, Quelennec *et al.*, in fact, took advantage of these features of HPT to study the homogenization of phase separated Cu-Fe alloys.[22] In that work, which we discuss later, the authors employed the ferromagnetism of Fe to relate the "degree" of atomic mixing to total strain. The current work also employs HPT in order to provide quantitative estimates of the relationship between forced chemical mixing and plastic strain. We select for this study, however, a eutectic Ag-Cu alloy since the experiments on this alloy can be quantitatively compared with the model of shear mixing proposed by Bellon and Averback.[23] This model assumes that atomic mixing is predominantly mediated through the unhindered glide of dislocations across interfaces.

Eutectic $Ag_{60}Cu_{40}$ alloys provide a model system for quantitative studies on forced chemical mixing for a number of reasons. First, the alloy phase separates on cooling from the melt into a well-defined lamellar structure.[24] Moreover, by controlling the solidification rate, the length scale of the phase separation can be kept well below 1 μm,[25] and uniform, thus allowing homogenization during HPT treatment. Second, molecular dynamics (MD) computer simulations have shown that at low temperatures, the forced mixing of Ag-Cu alloys behaves similarly to that of pure Cu. Significantly, dislocations transfer across interphase boundaries with little hindrance.[26,27] Thus, complications arising from large mismatches in the elastic properties, excessively large heats of mixing, or different crystalline structures (e.g., Cu-W, Cu-Nb, Cu-Fe) are avoided.[27] These simplifications enable direct comparison with computer simulations of shear-induced force mixing. Lastly, the Ag and Cu rich phases provide good contrast for x-ray diffraction (XRD) and transmission electron microscopy (TEM) since their different lattice parameters and atomic numbers make them easily distinguishable. In the following we first report the findings of the HPT shear mixing experiments, providing characterization of the microstructure and the amount of chemical mixing as a function of strain. We then use for comparison Monte Carlo simulations to calculate this same mixing function implementing the dislocation glide model of Bellon and Averback.[23] We use the simulations additionally to illustrate some of the consequences of the dislocation glide model on the morphology of the Ag-Cu interfaces as they evolve with strain.

II. EXPERIMENTAL PROCEDURES

High purity pellets of silver and copper (3.175 mm × 3.175 mm, Alfa Aesar, 99.99%) were used in the desired ratio to prepare the eutectic alloy with an atomic composition of $Ag_{60}Cu_{40}$. For this purpose, the pellets were repeatedly melted and cooled in an arc melter under purified argon atmosphere until a homogenous solid was obtained. The alloy was then cast into a water-cooled, cylindrical, copper mold, producing a cylindrical sample with a diameter of 5 mm and a length of 28 mm.

Specimens for HPT processing were obtained by cutting the alloy ingot into $\sim$ 1-mm-thick disks. The HPT processing was carried out using a Schenck testing machine, which has an axial load capacity of 400 kN in compression-torsion mode. The HPT deformation was conducted at room temperature by pressing the sample between two flat anvils (10 mm in diameter) while rotating the lower anvil against the upper under a compressive stress of 4.5 GPa. To increase the friction between the anvils and the sample and avoid slipping, the anvils were sand blasted prior to deformation. This creates a roughness of ≈ 1 μm. The angular range of rotation in the testing machine is limited to 90°, and therefore the torsional straining was performed in a cyclic manner, with each HPT cycle consisting of $+90^\circ$ (counterclockwise) followed by -90° (clockwise) rotations. The rotational speed was 1.2 turn/min (or 90° per 18 s). This process was repeated for a number of different cycles: $N = 1,3,5,10$, and 20, using different samples cut from the same ingot. After the HPT processing, the deformed samples were disklike, with a diameter of ≈ 10 mm and a thickness of ≈ 100 μm. This corresponds to a thickness reduction of $\sim 90\%$, which occurs mainly during the first cycle. We note that HPT is usually employed using a constrained geometry, whereby the sample thickness is not much changed.[21] We attempted such a geometry with our eutectic alloy samples but found that the strain was inhomogeneous, with shear mixing restricted to the top $\sim$ 10–20 μm on either side of the sample. Similar inhomogeneous straining during constrained HPT was reported previously in Cu.[28] No such inhomogeneities were found, however, using our flat anvils.

Microstructural evolution during HPT was characterized for selected samples using an aberration corrected TITAN 80-300 transmission electron microscope. TEM specimens were prepared by grinding, dimpling, and finally ion milling in a PIPS Gatan 691 using an energy of 3 keV. In order to monitor the distribution of the elements, energy dispersive x-ray spectroscopy (EDX) mapping was carried out in the STEM mode. A Philips X'Pert diffractometer equipped with a copper tube in Bragg-Brentano geometry operating at 45 kV/40 mA was used to characterize the phase evolution. The x-ray data were collected from an area of ~ 1.6 mm $\times 3$ mm near the edges of the disks. The evolution of phase formation during the HPT process was also investigated using differential scanning calorimetry (DSC) under flowing Ar atmosphere using a Netzsch DSC 204 F1 Phoenix at a heating rate of 10 °C/min. The samples for these measurements were comprised of 3 mm disks, which were punched out from the edge of HPT-processed samples.

III. RESULTS AND DISCUSSION

A. Experimental results

Figure 1(a) shows a TEM micrograph of the as-cast rapidly solidified $Ag_{60}Cu_{40}$ alloy and the corresponding selected area electron diffraction (SAED) pattern as an inset. The alloy is composed of alternating silver and copper lamellae, which is the typical microstructure of Ag-Cu eutectic alloys. The average thicknesses of the Ag and Cu lamellae are $\lambda_{Ag} \approx 120$ nm and $\lambda_{Cu} \approx 45$ nm, respectively. The SAED pattern in this figure also indicates a textured structure and a partial crystallographic orientation correlation between the lamellae of Ag and Cu. In Fig. 1(b) STEM/EDX elemental mapping across several lamellae shows sharp Ag/Cu interfaces as expected in this immiscible system. The grains in the as-cast sample are elongated along the lamellae, as seen in the dark-field TEM image of Fig. 1(c).

The primary control variable in HPT processing of materials at room temperature is the total plastic strain. In HPT-processed disklike samples, the accumulated shear strain increases linearly from the center to the circumference according to

$$\gamma = \frac{n\theta r}{t}, \tag{1}$$

where n is the number of cycles, θ is the rotation angle in each cycle (equal to π in the present experiments), r is the distance from the axis of rotation, and t is the thickness of the sample. In the present experiments, t decreased during the initial straining, but that is factored into the integral value of γ. Unless otherwise specified, the microstructural characterizations presented here were performed on specimens taken at a distance of $r \approx 3$ mm. At this position, the strain rate $\dot{\gamma}$ during the experiments was ≈ 1.5 s^{-1}.

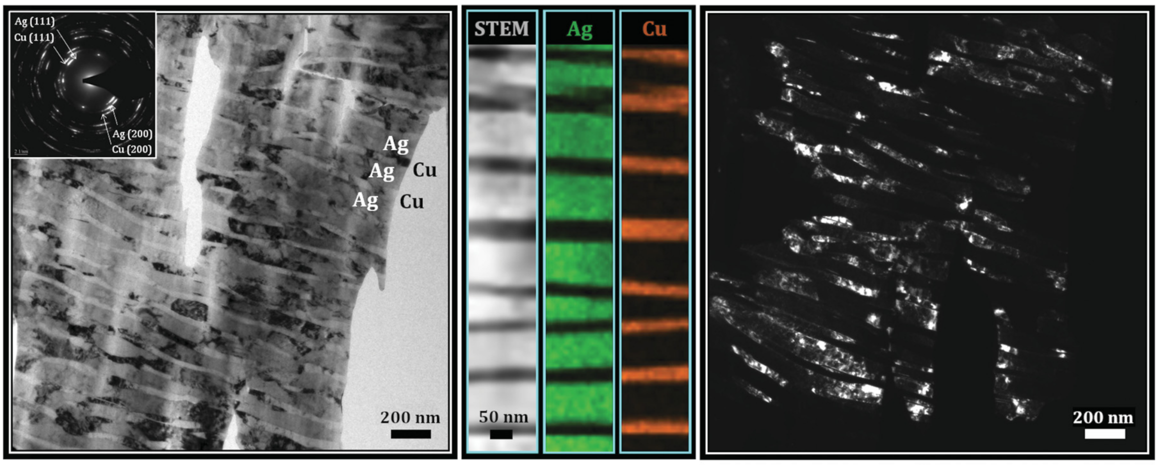

(a) (b) (c)

FIG. 1. (Color online) As-cast $Ag_{60}Cu_{40}$ eutectic alloy: (a) bright-field TEM micrograph and corresponding SAED pattern, (b) STEM/EDX elemental mapping across several lamellae, and (c) dark-field TEM image.

The x-ray diffractograms of the $Ag_{60}Cu_{40}$ alloy in the as-cast state and after different number of HPT cycles (1, 3, 5, 10, and 20 cycles) are shown in Fig. 2. After a single cycle, $\gamma \approx 41$, a new peak/shoulder appears adjacent to the main Ag peak at higher scattering angles. The intensities corresponding to the Cu-rich phase continuously diminish. This trend continues as the number of cycles is increased to 3 ($\gamma \approx 141$). After five cycles ($\gamma \approx 295$) the diffraction pattern indicates that a single fcc phase remains, although the (111) and (200) peaks have broadened considerably from the original Ag and Cu peaks. Additional straining to 10 and 20 cycles ($\gamma \approx 725$ and 1885, respectively) results in little additional change in the diffraction pattern in comparison to that shown after five cycles. The lattice parameter deduced from the main diffraction peak obtained for the sample processed for ten cycles is 3.94 Å; this value agrees with that reported for a $Ag_{60}Cu_{40}$ solid solution obtained by rapid melt quenching.[29]

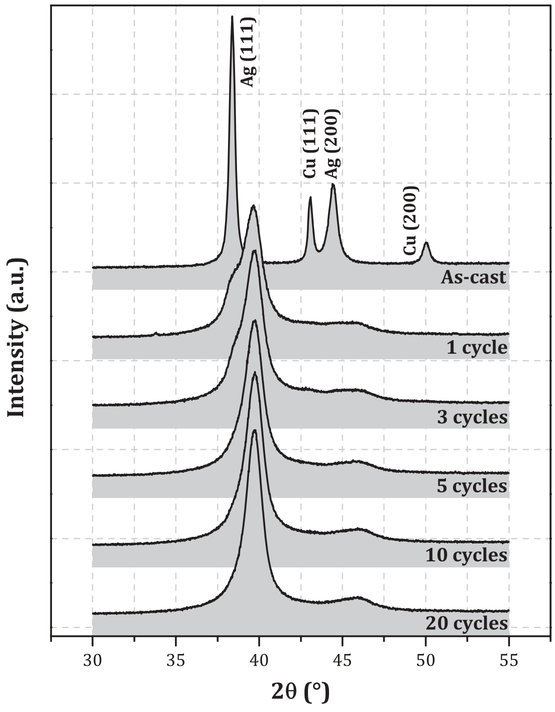

FIG. 2. X-ray diffractograms of $Ag_{60}Cu_{40}$ eutectic alloy in the as-cast state and after different number of HPT cycles.

The evolution of the phase formation was examined more quantitatively by performing DSC measurements on the HPT processed samples. The DSC traces of the alloy following different numbers of HPT cycles are shown in Fig. 3(a), while Fig. 3(b) plots the stored enthalpy as a function of strain. The maximum heat flow is detected for each curve at about 220 °C (using a heating rate of 10 °C/min). Homogenization of the alloy appears complete by ≈ 10 cycles. The stored enthalpy in the sample after this level of strain is ≈ 5.5 kJ/mol. This value is in good agreement with that obtained during cryomilling of a $Ag_{50}Cu_{50}$ alloy, 5.6 kJ/mol; the peak temperature for the heat evolution also agrees well with that work.[30] Since the average grain size after HPT is ≈ 42 nm (see below), no correction for grain growth was necessary.[30] According to Ref. 30, moreover, grain growth takes place at higher temperatures $T \sim 300\,^{\circ}\mathrm{C}$. For later comparison with the simulation, we define a characteristic experimental strain for homogenization γ_e. This strain is obtained from the DSC measurements by linearly extrapolating the low strain region of the stored enthalpy curve to high strains as indicated in Fig. 3(b). The initial rapid increase in the stored enthalpy below 1 cycle is presumably due to some nonhomogeneities (more refined regions) in the microstructure and possibly associated with the thinning of the sample during this first cycle. This procedure yields $\gamma_e \approx 350$.

Figure 4(a) shows a STEM image of the sample after ten cycles, while Fig. 4(b) shows STEM/EDX elemental mapping of the marked area. As shown, the microstructure is no longer composed of Ag/Cu lamellae; instead the two elements are distributed homogeneously throughout the microstructure. A dark-field image from this sample and the corresponding SAED pattern are shown in Fig. 4(c). HPT has also led to the formation of equiaxed grains that have an average size of ≈ 42 nm. No Debye-Scherrer rings related to pure Ag or Cu appeared in the SAED pattern. The lattice spacings calculated for the rings of the new fcc structure yield a lattice parameter of

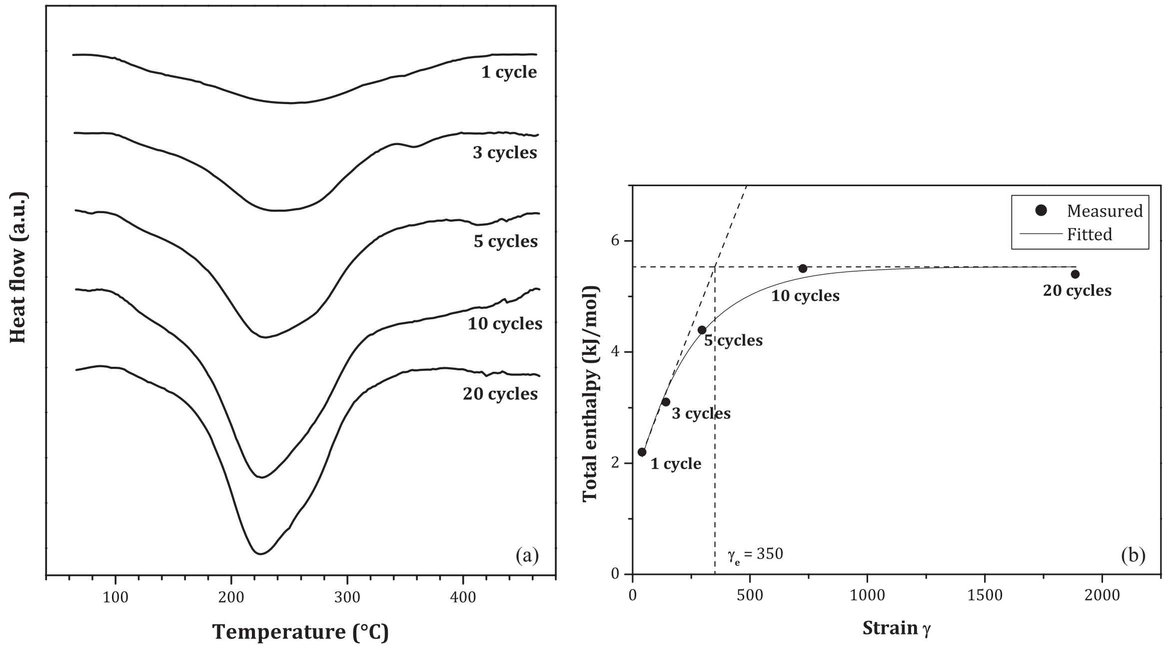

FIG. 3. DSC results of $Ag_{60}Cu_{40}$ eutectic alloy after different number of HPT cycles: (a) DSC scans, and (b) total stored enthalpy plotted as a function of strain.

3.96 Å, which agrees with the XRD results. These results, taken together, clearly indicate the formation of a homogeneous nanocrystalline, supersaturated, solid solution of Ag and Cu.

Similar characterization was performed on a specimen taken from the center of the HPT disk deformed to ten cycles. The STEM overview together with the corresponding SAED pattern and a bright-field image of the marked area in this image are shown in Figs. 5(a) and 5(b), respectively. We emphasize that the strain at this location is far smaller [see Eq. (1)], although, the precise amount of strain is difficult to quantify since the exact location r of the electron transparent area is uncertain to within $\approx 300\ \mu$m. Nevertheless, the SAED pattern in Fig. 5(a) provides clear evidence that the original Ag-Cu lamellar structure remains largely intact. Comparison of the microstructures shown in Fig. 5 ($r \approx 0$ mm) with those in Fig. 4 ($r \approx 3$ mm) illustrates the immense microstructural differences within the HPT-processed disk.

Comparison of the SAED patterns in Figs. 1(a) and 5(a) also reveals that significant grain refinement has taken place at the center of the disk even though no significant interdiffusion between Ag and Cu lamellae has occurred (also confirmed by high resolution TEM, but not shown here). Moreover, the overall geometry of the lamellae near the center of the specimen also differs from that in the as-cast condition. The

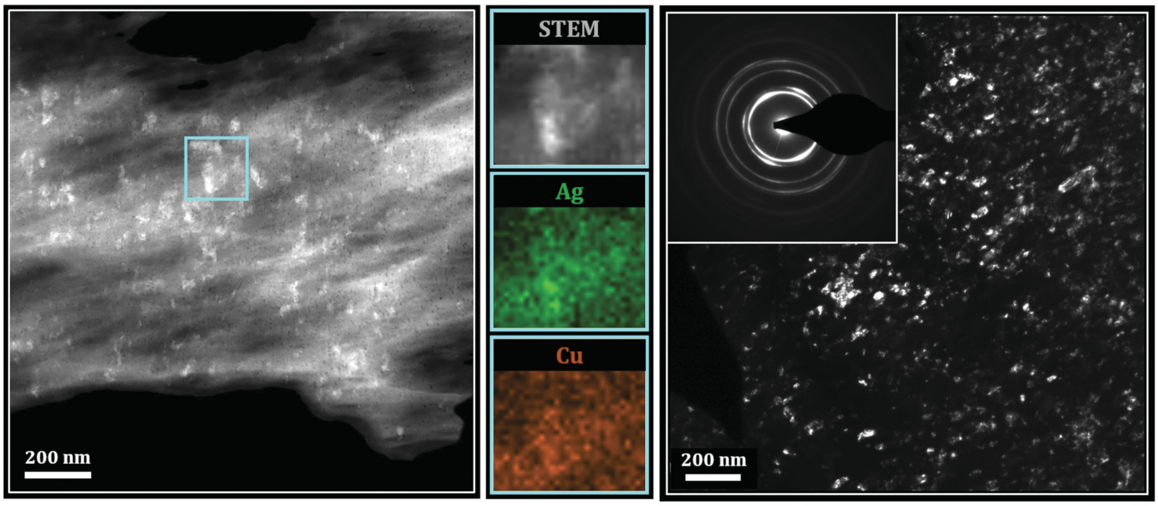

(a) (b) (c)

FIG. 4. (Color online) Transmission electron micrographs of a disk processed by HPT for 10 cycles: (a) STEM overview, (b) STEM/EDX elemental mapping of the marked area in (a), and (c) dark-field image and corresponding SAED pattern.

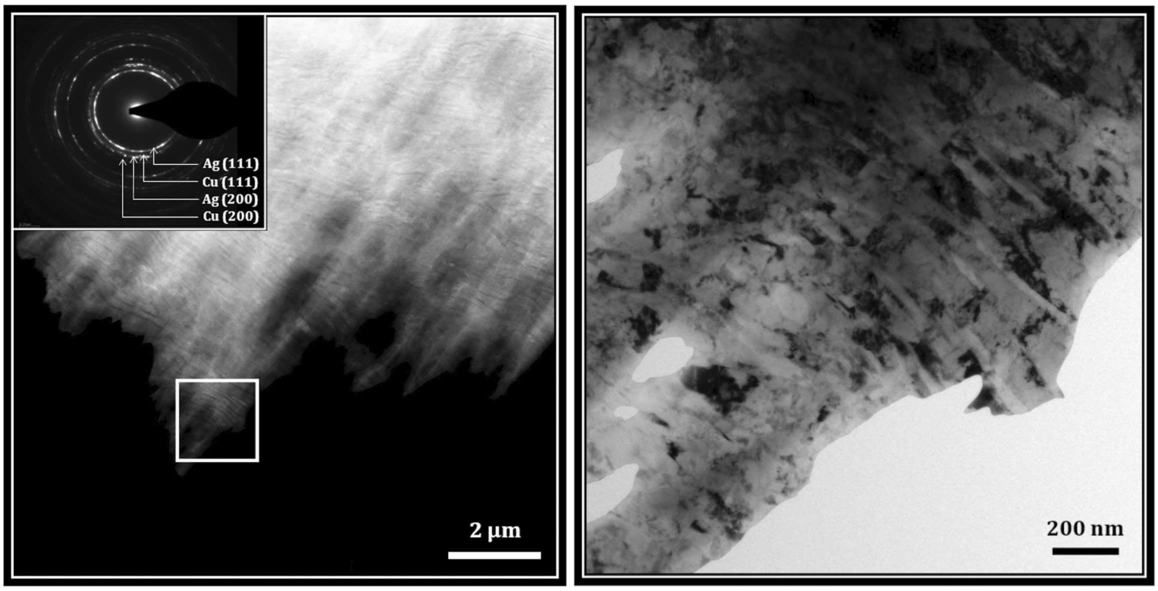

(a) (b)

FIG. 5. (a) STEM overview from the center of a disk processed by HPT for 10 cycles and corresponding SAED pattern, and (b) bright-field image of the marked area in (a).

interfaces between the two metals also appear rougher and less straight. More importantly, the wavelength of lamellar spacing is reduced to ~ 30 nm. This reduction appears associated with the decrease in specimen thickness from 1.0 to ~ 0.1 mm during the first HPT cycle. We performed XRD on the center of the sample after the first cycle and determined average layer thicknesses of ≈ 16 nm for the both Ag and Cu layers using the Scherrer equation, in agreement with the value determined by TEM.

B. Model of shear mixing: Monte Carlo simulations

The effect of shear deformation on the lamellar structure of the eutectic Ag-Cu system was simulated using a modification of the Monte Carlo (MC) technique originally employed by Bellon and Averback.[23] In the earlier work, kinetic MC was employed to examine the competition between disordering, due to shear, and ordering due to vacancy motion. Their model assumes that mixing results from the passage of dislocations through a crystal in which the two phases are crystallographically coherent. MD simulation has since shown that this is a reasonable approximation for two-phase Ag-Cu alloys.[27] The present work thus uses this model to calculate the homogenization rate of Ag-Cu alloys, for comparison with the experiments. We also use the model to examine the dynamics of shear mixing and its effect on the interface morphology. Strain is achieved by passing pairs of dislocations with opposite Burgers vectors through the crystal. Pairs are used, rather than single dislocations, to satisfy the periodic boundary conditions of the computational cell. A series of samples was created with the largest sample consisting of a fixed fcc lattice with $724 \times 724 \times 724$ atoms in a rhombohedral cell, out of which 217 contiguous (111) planes are Cu and the rest Ag. This number of planes closely corresponds to the number in the as-cast eutectic alloy shown in Fig. 1(a). Since the cell is coherent, rather than semicoherent as in the experiment, the composition is somewhat different, 70:30 compared to 60:40 in the experiment. Other cells, with eutectic periods reduced in thickness by factors of 2, 4, 6, and 10 were also examined to investigate how the rate of homogenization scales with the length scale of the microstructural features.

Each pair of dislocations passing through the sample results in a stack of $\{111\}$ planes being shifted in-plane by one atomic distance in a $\langle 110 \rangle$ direction. This results in a shear strain increment per dislocation of $\sqrt{3/2}$ divided by the number of planes in the simulation cell. The number of planes in the stack, the location of the stack, and the particular $\langle 110 \rangle$ direction are all selected randomly. The forced mixing in the simulation cell is characterized by a short range order (SRO) parameter Ω calculated from the numbers of Cu-Ag, Cu-Cu, and Ag-Cu nearest neighbor bonds,[31]

$$\Omega = \frac{\frac{c}{1-c} N_A^B + \frac{1-c}{c} N_B^A}{N_A^A + N_B^B} - 1. \tag{2}$$

An order parameter of -1 represents a fully phase-separated system, 0 represents a random solution, and $+1$ represents an ordered alloy. While the procedure just described is straightforward to implement in MC simulations, and described earlier by Bellon and Averback,[23] it is not practical for the large size of the simulation cell required here and hence an alternative procedure was employed. The new method creates a list of all the shearing events that would be carried out in a kinetic MC code, in their proper order, but it does not execute these shears. Rather, it assumes that the crystal is in its final sheared state, with the identities of all atoms unknown. The code next uses the list of shearing events in reverse order, to track randomly chosen pairs of nearest neighbor atoms back to their origin and thereby determine their identity. A statistical sample of the disorder is thus obtained, and it allows analysis of arbitrarily large samples and strains, independent

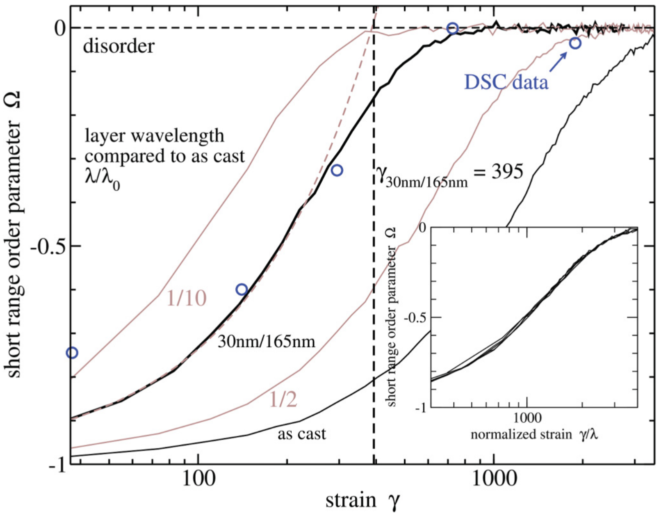

FIG. 6. (Color online) SRO parameter as a function of shear strain for four eutectic wavelengths of the Ag-Cu bilayer sample as determined from MC simulation (solid lines). The as-cast curve corresponds to the experimental sample, consisting of $\lambda = \lambda_0 = 724$ atomic layers with 30% Cu in a contiguous layer. The dashed line on curve marked 30 nm/165 nm is an extrapolation of the data assuming exponential mixing. Inset shows the SRO parameter plotted versus normalized strain. Symbols represent experimental data from Fig. 3(b); they were converted to SRO parameters assuming a regular solution model.

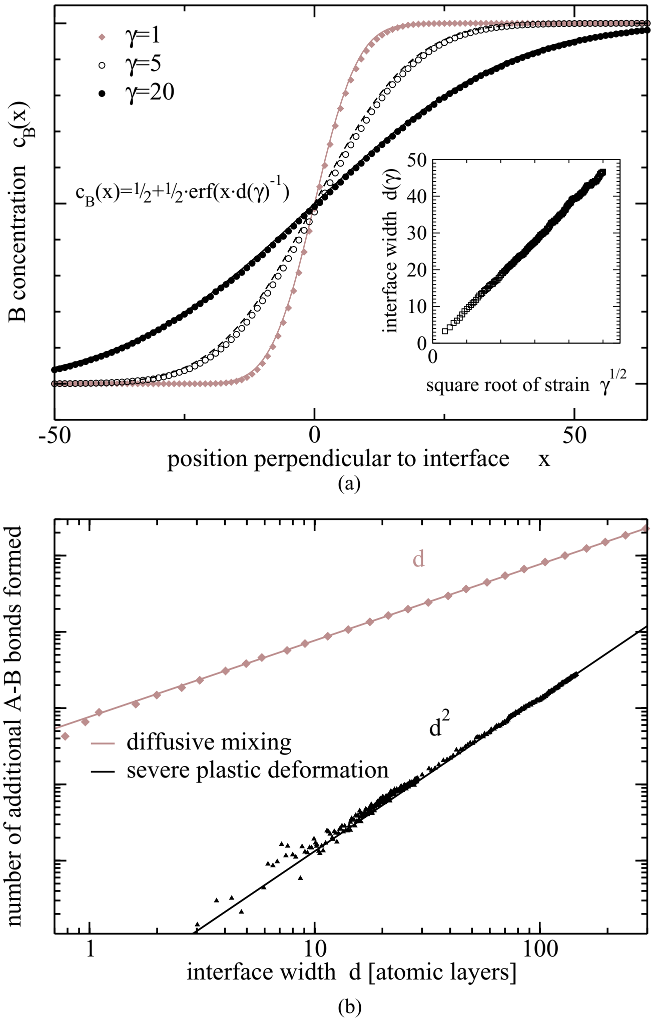

FIG. 7. (Color online) (a) The simulated concentration profile of solute atoms across an interface is plotted for strains γ of 1, 5, and 20. The data points (symbols) are fitted with an error function (lines). The inset shows the interface width, obtained from the fitting parameter d, as a function of the square root of the applied strain. (b) Number of A-B bonds plotted as a function of the interface width for shear mixing and diffusive mixing.

of computer memory and CPU power since atom locations after each shearing event need not be stored.

Figure 6 is a plot of the SRO parameter for four eutectic wavelengths as a function of shear strain up to 3500. The first result of these simulations is that the strain calculated for homogenization of eutectic structure with wavelength =165 nm, using the same procedure employed for the experimental value, is $\gamma_{\text{sim}} \approx 2200$. This value is considerably higher than the experimental value $\gamma_e \approx 350$, but we discuss this comparison in detail later. Before that, however, we examine the dependence of γ_{sim} on the wavelength of the lamellar structure. Figure 6 shows that the strain required for homogenization scales linearly with wavelength λ and not as λ^2, as would be expected for Fickian diffusion. This result agrees with a previous study on the dissolution of spherical precipitates using MD computer simulations, which had shown that shear mixing is superdiffusive, and that the strain required to dissolve small spherical precipitates of radius R_p scales with $1/R_p$, which again is distinct from the $1/R_p^2$ scaling for Fickian diffusion.[32] For multilayered structures, for example ARB, the signature of superdiffusive mixing is far more subtle and it could lead to incorrect conclusions being drawn from experimental studies of the mixing process, as we briefly illustrate.

To investigate the dynamics of the shear mixing process, simulations of isolated interfaces were performed. This was achieved by increasing the layer period sufficiently so that neighboring interfaces do not interact within the observed range of mixing intensities. The observed interfaces were thus indistinguishable from interfaces between two semi-infinite half-spaces. At regular time intervals during these simulations we obtained a concentration profile perpendicular to the interface, by calculating the solute concentration in each atomic plane parallel to the interface. The shape of the concentration profile across the interface could be fitted with an error function, with the only free parameter being the width of the interface. Figure 7(a) shows three such concentration profiles, obtained by averaging several hundred sheared interfaces. Plotting the fitted width of the sheared interface as a function of the square root of strain $\gamma^{1/2}$, a linear dependence is observed, which at constant strain rate translates to a *square root of time* $t^{1/2}$ dependence. This behavior is thus superficially identical to diffusive mixing. This result is not unexpected, however, since by shifting planes randomly normal to the interface, the atoms perform a random walk. Motion transverse to the interface does not affect the average concentration of each plane parallel to the interface. This leads to the important conclusion that shear mixing cannot be distinguished from diffusive mixing by simply measuring average concentration profiles across interfaces.

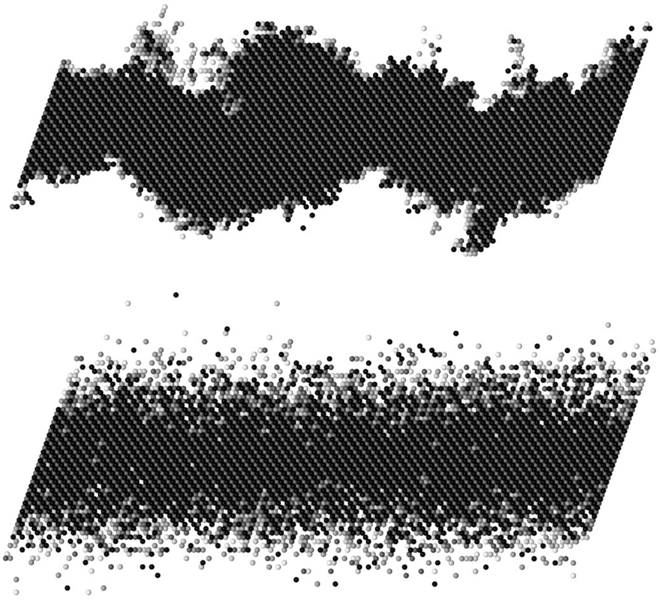

FIG. 8. Cross sectional views of atoms, subjected to shear mixing (top) or diffusive mixing (bottom). Shear mixing leads to predominantly low frequency roughening of the interfaces compared to the atomic scale disorder introduced by diffusive mixing. Grayscale indicates distance from the cut plane.

The differences between shear and diffusive mixing become obvious on examining the chemical order. For this purpose we performed additional *control* simulations in which we swapped the chemical identities of a set of random atoms with one randomly chosen nearest neighbor of each. This models a diffusive mixing process that lacks the long-range correlations introduced by dislocation glide. Counting the number of additionally introduced A-B bonds as a function of interface width for the two mixing mechanisms shows very distinct dependencies, as seen in Fig. 7(b). The simulation of the sample mixed by SPD exhibits a d^2 dependence of newly created A-B bonds on the observed interface width d, while the sample subjected to diffusive mixing shows the expected linear dependence of created bonds versus d. Since the interface width increases as the square root of time for both diffusive and the superdiffusive shear mixing, as described above, we obtain the result that the chemical disorder increases linearly in time for shear mixing, but only as the square root of time for diffusive mixing.

The superdiffusive character of shear mixing also has significant consequences for the structure of the interface. Notice that the number of bonds produced by shear mixing is far less than that for diffusive mixing [Fig. 7(b)] for a given interface width. This can be understood by looking at the actual microstructures along the interfaces for the two types of mixing. These are shown in Fig. 8, where it is seen that the correlations in atomic motion produced by dislocation glide introduce roughness predominantly at large wavelengths. This leads to a "wavy" interface with little diffuseness, while regular diffusion creates a flat interface that is diffuse. It is noteworthy that the interface structure observed in the HPT experiments near the position $r = 0$ (Fig. 5), where the strain is relatively small, also revealed a wavy character. Additional experiments will be necessary, however, to confirm whether this waviness indeed reflects the superdiffusive character of SPD.

We now return to the comparison between the experimental and calculated values of strain required for homogenization. As noted above, $\gamma_e \approx 350$ while $\gamma_{\mathrm{sim}} \approx 2200$. The determination of γ_{sim}, however, assumed that the wavelength of the eutectic structure was 165 nm; its value in the original structure. Since the HPT experiments employed an unconstrained geometry, as mentioned earlier, the sample thickness became smaller at the very early stages of the HPT processing. By the end of the first cycle, the thickness had decreased by nearly a factor of 10. As noted above, Fig. 5 shows that at the center of the sample, which had been compressed but only slightly strained, the lamellar spacing was reduced to $\lambda \sim$ 30 nm; this value also agreed with that determined by the peak broadening using XRD from the center of the sample after one cycle. If we thus assume a lamellar wavelength of 30 nm, we now find that the agreement between the experiments and the simulations is quite good, as $\gamma_{\mathrm{sim}} \approx 400$. This is seen in Fig. 6 where the experimental points from the DSC measurements fall very close to the simulation curve representing a wavelength of 30 nm. Conversion of the experimental DSC data in Fig 3(b) to short-range order parameters assumes a regular solution model. While this close agreement between simulation and experiment must be considered somewhat fortuitous, given both the uncertainty in the eutectic wavelength due to compression and the simplicity of the shearing model, it nevertheless provides good support for the proposed model of mixing in Ag-Cu, that is, shear mixing in systems like Ag-Cu can be explained entirely by dislocation glide. Models involving diffusion are unnecessary to explain these results.

Lastly we comment on the HPT shear mixing of Cu-Fe reported in the literature.[22] The samples in that study were prepared by wire drawing. While the microstructure was not uniform, the Fe filaments were specified to have an average diameter of $\approx$ 30 nm, and they required a shear strain of ≈ 540 for homogenization (we multiply the average Fe filament diameter quoted 50 nm by the reduction in the thickness of the disk—60%.) This value is of similar magnitude to our value of $\gamma_e \approx 350$. Whether the close agreement is fortuitous is presently unclear. Recent MD simulations of shear mixing of 6 nm Fe nanoprecipitates in Cu, however, provide some perspective on this question. These simulations have shown that the Fe nanoparticles become (semi-) coherent in Cu during straining, and when this occurs, dislocations can transfer across the Fe-Cu interface; shear mixing then becomes superdiffusive and the mixing is similar to Ag-Cu.[27] On the other hand, when the Fe particles are not aligned with the Cu matrix, that is, early in the shearing process, dislocations do not transfer across interfaces and the mixing is diffusive. The MD simulations further showed that in this latter case, when the mixing is diffusive, mixing is anisotropic; Fe mixes into the Cu but only little Cu dissolves into Fe. This finding is consistent with the results reported in Ref. 22. Thus it is presently difficult to assess the extent to which the mixing in Cu-Fe is superdiffusive in this alloy, however, it appears that at the early stages of shearing, the mixing is diffusive, and only later when the Fe filaments become refined, the shearing mixing becomes superdiffusive.

IV. CONCLUSION

A quantitative measurement of the relationship between forced chemical mixing and plastic strain was performed on a Ag-Cu eutectic alloy using HPT deformation. The experiments revealed that HPT on this alloy, using a constrained geometry, leads to highly nonhomogeneous deformation. The deformation is homogeneous, however, for an unconstrained geometry, but the sample becomes much thinner. The measurements showed that the initial eutectic wavelength of $\approx$ 165 nm is effectively reduced to $\approx$ 30 nm during the first cycle in the HPT, where $\gamma \approx 20$, and that the strain required for homogenization $\gamma_e \approx 350$. The experiments also indicated a textured structure and partial crystallographic orientation correlation between the Ag-rich and Cu-rich lamellae. MC computer simulations showed that a very simple model of forced chemical mixing can reasonably account for the rate of homogenization with strain. The simulations further revealed that strain required for homogenization should scale linearly with the length scale of the initial inhomogeneity, owing to the superdiffusive mixing produced by dislocation glide.

ACKNOWLEDGMENTS

The research at TUD and KIT was financially supported by Deutsche Forschungsgemeinschaft (DFG) under the Project HA1344/23-1 and at the University of Illinois by the US National Science Foundation under Grant DMR 10-05813 and the US Department of Energy, Basic Energy Sciences under Grant DOE LANL 76604-001-10 (EFRC-CMIME). The experimental support by Dr. Julia Ivanisenko (Institute of Nanotechnology, KIT) and Dr. Holger Gesswein (Institute of Applied Materials, KIT) is gratefully acknowledged. The authors are also grateful to the Institute of Applied Materials at KIT for access to the Schenck compression-torsion machine, and to Stefan Knaak for assistance in conducting the HPT process.

---

[1] See, e.g., R. B. Schwarz and C. C. Koch, Appl. Phys. Lett. **49**, 146 (1986).

[2] See, e.g., A. Sagel, H. Sieber, H. J. Fecht, and J. H. Perepezko, Acta Mater. **46**, 4233 (1998).

[3] D. Raabe, S. Ohsaki, and K. Hono, Acta Mater. **57**, 5254 (2009).

[4] D. A. Rigney, Wear **245**, 1 (2000).

[5] J. L. Young, Jr., D. Kuhlmann-Wilsdorf, and R. Hull, Wear **246**, 74 (2000).

[6] C. G. Rhodes, M. W. Mahoney, W. H. Bingel, R. A. Spurling, and C. C. Bampton, Scr. Mater. **36**, 69 (1997).

[7] P. E. Van Keken and S. Zhong, Earth Planet. Sci. Lett. **171**, 533 (1999).

[8] C. Gente, M. Oehring, and R. Bormann, Phys. Rev. B **48**, 13244 (1993).

[9] F. Delogu, M. Pintore, S. Enzo, F. Cardellini, V. Contini, A. Montone, and V. Rosato, Philos. Mag. B **76**, 651 (1997).

[10] J. Xu, U. Herr, T. Klassen, and R. S. Averback, J. Appl. Phys. **79**, 3935 (1996).

[11] E. Botcharova, J. Freundenberger, and L. Schultz, J. Mater. Sci. **39**, 5287 (2004).

[12] A. R. Yavari, P. J. Desré, and T. Benameur, Phys. Rev. Lett. **68**, 2235 (1992).

[13] R. B. Schwarz, Mater. Sci. Forum **269-272**, 665 (1998).

[14] M. Angiolini, G. Mazzone, A. Montone, and M. Vittori-Antisari, Mater. Sci. Forum **235-238**, 175 (1997).

[15] R. J. Hebert and J. H. Perepezko, Scr. Mater. **50**, 807 (2004).

[16] X. Sauvage, D. H. Ping, D. Blavette, and K. Hono, Acta Mater. **49**, 389 (2001).

[17] A. Bachmaier, M. Kerber, D. Setman, and R. Pippan, Acta Mater. **60**, 860 (2012).

[18] C. Suryanarayana, Prog. Mater. Sci. **46**, 1 (2001).

[19] D. R. Maurice and T. H. Courtney, Metall. Trans. A **21**, 289 (1990).

[20] F. Delogu, G. Mulas, L. Schiffini, and G. Cocco, Mater. Sci. Eng. A **382**, 280 (2004).

[21] A. P. Zhilyaev and T. G. Langdon, Prog. Mater. Sci. **53**, 893 (2008).

[22] X. Quelennec, A. Menand, J. M. Le Breton, R. Pippan, and X. Sauvage, Philos. Mag. **90**, 1179 (2010).

[23] P. Bellon and R. S. Averback, Phys. Rev. Lett. **74**, 1819 (1995).

[24] T. B. Massalski, *Binary Alloy Phase Diagrams*, 2nd ed. (ASM International, Materials Park, Ohio, 1990), p. 28.

[25] T. D. Shen, R. B. Schwarz, and X. Zhang, Appl. Phys. Lett. **87**, 141906 (2005).

[26] S. Odunuga, Y. Li, P. Krasnochtchekov, P. Bellon, and R. S. Averback, Phys. Rev. Lett. **95**, 045901 (2005).

[27] See, e.g., Y. Ashkenazy, N. Q. Vo, D. Schwen, R. S. Averback, and P. Bellon, Acta Mater. **60**, 984 (2012).

[28] C. J. Shute, B. D. Myers, Y. Liao, S.-Y. Li, A. M. Hodge, T. W. Barbee, Jr., Y. T. Zhu, and J. R. Weertman, Scr. Mater. **65**, 899 (2011).

[29] R. K. Linde, J. Appl. Phys. **37**, 934 (1966).

[30] T. Klassen, U. Herr, and R. S. Averback, Acta Mater. **45**, 2921 (1997).

[31] A. C. Lund and C. A. Schuh, Phys. Rev. Lett. **91**, 235505 (2003).

[32] P. Bellon, R. S. Averback, S. Odunuga, Y. Li, P. Krasnochtchekov, and A. Caro, Phys. Rev. Lett. **99**, 110602 (2007).